express
polymer letters

Research article

Influence of 3D printed structures on energy absorption ability of brittle polymers under dynamic cyclic loading

Mohit Sood [ID] *, Chang-Mou Wu* [*] [ID]

Department of Materials Science and Engineering, National Taiwan University of Science and Technology, 10607 Taipei, Taiwan, R.O.C

Abstract. Structural change can alter the energy absorption ability of constituent materials. Carbon organic framework (COF)-inspired structures printed with fusion deposition modeling (FDM) using polylactic acid (PLA) and acrylonitrile butadiene styrene (ABS) polymers are used to analyze the structural effect. Structures were characterized for specific energy absorption under static compression. The best structures from the static testing results were further characterized for dynamic compression using sinusoidal displacement to calculate the dynamic elastic recovery (DER), hysteresis work, and $\tan\delta$. Based on the results, the bending-dominated structure absorbed the highest energy, and the surface structure provided the best DER. The structure which failed by the pure collapsing of the layer showed the best specific values. The delamination of printed layers during loading reduced the performance of structures despite of the materials.

Keywords: processing technologies, mechanical properties, material testing, fusion deposition modeling, polymer

1. Introduction

Several manufacturing techniques for instant casting, forging, welding, and forming have been used for decades. However, industries are now shifting their focus toward additive manufacturing (AM) because of its ability to manufacture lightweight and structural designs [1, 2]. Currently, AM has been employed to fabricate numerous engineering components using polymers and metallic materials. Vat photopolymerization, material jetting, material extrusion, sheet lamination [3, 4], direct energy deposition binding jets, and powder bed fusion [5–10] are examples of commercially applied AM processes.

Among the processes, fusion deposition modeling (FDM) is widely used to create three-dimensional (3D)-printed structures using thermoplastic filaments [11]. FDM provides manufacturing with greater autonomy to control mechanical properties [12]. These properties are easy to alter by changing

some parameters, such as the extrusion and printing bed temperature, printing speed [12–15], resolution of the extruded layer, infill density, and pattern [15, 16]. This makes FDM more suitable for fabricating lattice structures. Polylactic acid (PLA) and acrylonitrile butadiene styrene (ABS) are abundantly available commercial polymeric materials [17–21]. These polymers are well known for their high mechanical strength, better printability at a low cost, and biodegradable nature for PLA, which make them suitable candidates for lattice structure fabrication using FDM [22–25].

In recent years, researchers have fabricated traditional structures and analyzed their compression properties. Dalaq *et al*. [26] fabricated a triply periodic minimal surface (TPMS) of the Schwarz structure, diamond rhombic, Schoen, Neovius, and Fischer–Koch types using Tango- and Vero-plus material and evaluated the mechanical properties under uniaxial compression.

---

*Corresponding author, e-mail: cmwu@mail.ntust.edu.tw

They concluded that the Schwarz primitive showed the best mechanical properties because of least debonding under static loading [26]. Honeycomb structures using thermoplastic polyurethanes were manufactured by Bates *et al.* [27] They concluded that the energy absorption ability of these structures depended on the strain rate and cell orientation of the structure under the static compression load. Li *et al.* [28] proposed truss, conventional honeycomb, and re-entrant honeycomb structures and evaluated their bending behavior. Owing to the localized stress concentration in the truss and conventional honeycomb structures, they showed an early catastrophic failure. Hence, the energy absorption and mechanical properties were less than that of the re-entrant structure Abueidda *et al.* [29] printed Schwarz, Schoen, and Neovius structures with polyamide-12 and evaluated their compressive strength, modulus, and energy absorption with static loading. The Neovius structure provided the highest results because it retained the geometrical structure until the compression ended [29]. Cubic, octet, and Isomax structures were characterized by quasi-static bending and dynamic low-velocity impact. The Isomax with cubic meta sandwich beam provided the highest energy absorption under bending as well as impact [30]. Al-Ketan *et al.* [31] evaluated the mechanical properties of the strut base, skeletal-TPMS, and sheet-TPMS structures under uniaxial static compression, and the high relative density of the sheet-based TPMS structures outperformed that of the other structures. Another report by Abueidda *et al.* [32] evaluated the mechanical properties of the gyroid surface structure under a uniaxial static test and demonstrated that the highest relative density absorbed the highest amount of energy under static compression. Similarly, octet structures composed of PLA were found to absorb more specific energy at a higher relative density under quasi-static compression [33]. Evidently, most studies were performed using static loading compression, and none has yet used dynamic compression yet, particularly not with sinusoidal displacement for the characterization of the proposed structures.

Most studies have focused on traditional TPMS and octet structures, and for these structures, relative density is the most effective criterion for good energy absorption. However, if a greater number of strut arrangements are provided in the loading direction, the energy absorption ability of the structure may also be enhanced. Carbon organic framework (COF)

compounds have some unique two-dimensional and 3D atom arrangements that can be used as inspiration for designing novel structure arrangements because they can provide more struts in the loading direction [34–37]. These COF-inspired structures fabricated using FDM with PLA and ABS have never been reported. The main aim of this study is to fabricate the proposed COF-inspired structures printed with hard materials (PLA and ABS) and characterize the effect of these structure arrangements on the energy absorption ability of the materials under static and dynamic sinusoidal cyclic loading compression.

2. Experimental procedure
2.1. Design of structures
The design concept for the new type of structure was inspired by the COF compounds shown in Figure 1. The major advantage of COF-inspired structures is their ability to change the density of unit cells without changing in diameter, and all inspired structures can provide more struts in the loading direction.

The lattice structures are either strut or surface-based and show stretch or bending domination behaviors [2]. COF compounds have an umpteen type of atomic arrangements that can be used to fabricate both types of structures. The first structure (S1) was drawn from the sp^2 carbon conjugate COF. This compound can provide the stretch domination behavior (Maxwell number (M) = 5) by dividing the load on the two struts. The S2 and S3 structures were adopted from the boronic ester and tetrathiafulvalene COFs. These arrangements were selected because they can provide the bending domination behavior ($M = -6$ for S2 and $M = -12$ for S3). To compare the strut-based structure with surface-typed structures, periodic surface-based structures (SS) were designed by mimicking the zeolitic imidazolate framework (ZIF-8). The SS can provide better foam-like properties. Another reason for the selection of these COF compounds was their printability with the FDM printer. All unit cells of the inspired structures carry loads, as shown in Figure 2.

Solidworks 2019 (SP5, Dassault Systèmes, Vélizy-Villacoublay, France) was used to illustrate the CAD files of the structures. The structures were formed according to the hybrid connection approach as outlined in Figure 3. A unit cell of 10×10×10 mm was formed in two manners: with an external connector and with self-connection. This approach can control the density of the unit cell without changing the diameters of the struts. The external connector made
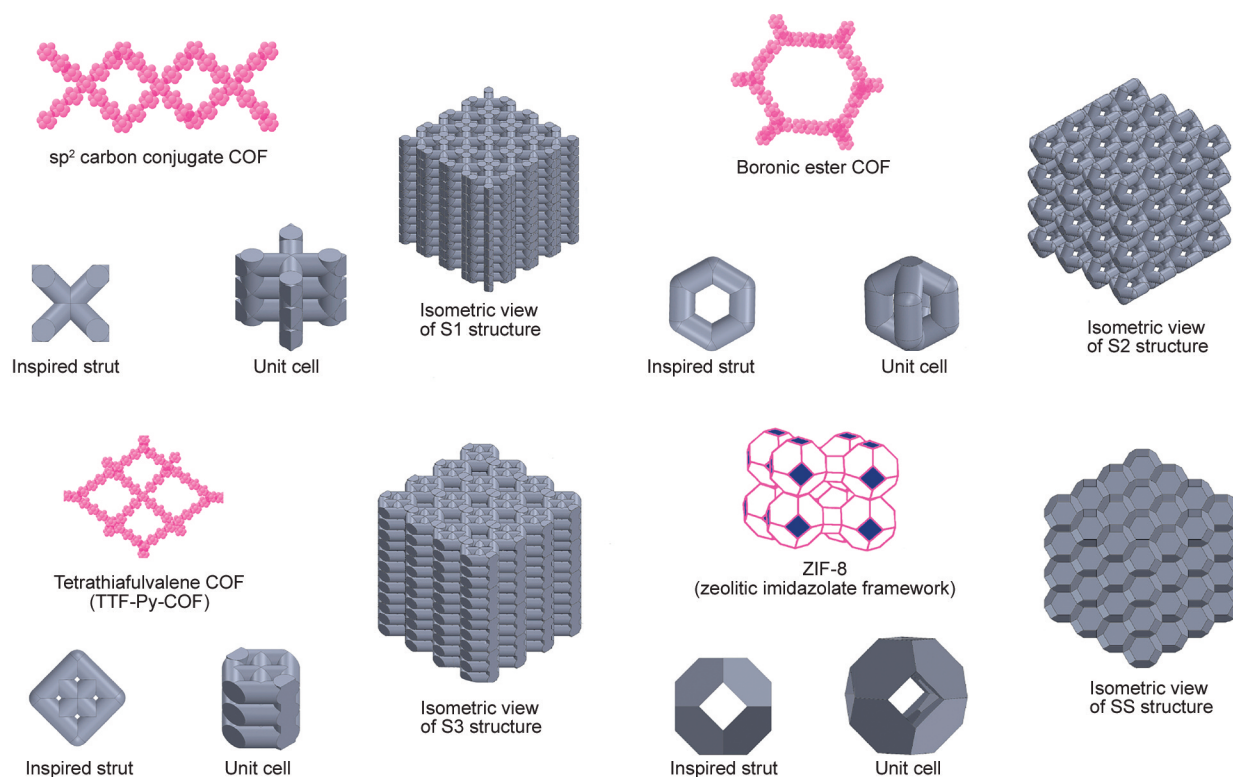
Figure 1. Unit cells inspired by the different carbon organic frameworks, along with final structural arrangements.
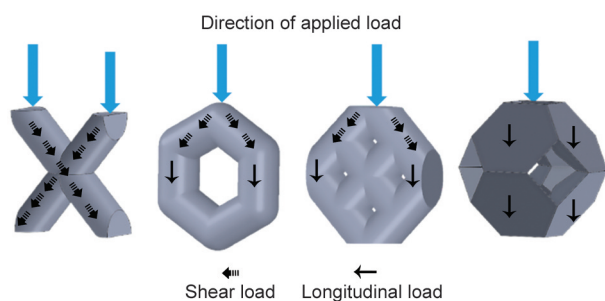
Figure 2. Direction and distribution of the load in the struts and shell-type unit cells under the compression loading.

the unit cell denser, whereas self-connection made the unit cell more porous. Unit cells were repeated in the 3D space to form 40 × 40 × 40 mm [35] structures. All unit cells were connected with the surfaces in the 3D structure. The diameter for the struts was selected to be 3.00 mm, which is the minimum diameter that prints at an acceptable quality. Similarly, the SS was printed with a 3.00 mm shell.

2.2 Manufacturing samples

All printing filament materials: ABS (PA-756, POLYLAC®, Chimei Corporation, Tainan, Taiwan) and PLA (4032D, IngeoTM, NatureWorks, Minnesota, USA; having D-lactic content of 1.4%), were purchased from XYZ Printing Company, Taipei, Taiwan, with a diameter of 1.75 mm. The CAD drawing of

these samples was saved in STL format and sliced using Ultimaker Cura 4.13 software (Ultimaker B.V., Massachusetts, USA). The G-codes, generated with Cura, were sent to the 3D printer (Ender-3 Max, Creality 3D technology corporation limited, Shenzhen, China) with a nozzle diameter of 0.4 mm. Table 1 lists the optimized printing parameters.

2.3. Morphology of structures

To verify the printing quality and layer adhesion of the manufactured samples, one unit of each type of structure was examined randomly under an optical microscope (SV-55, Sage Vision, Pennsylvania, USA). For further investigation of the quality of fabricated structures, the higher magnification images were captured by a scanning electron microscope (SEM, 6390 LV, JEOL, Tokyo, Japan). As all the samples were non-conductive, hence, before keeping them inside the SEM chamber, the platinum coating was applied by using an automatic spin coater (JFC-1300, JEOL, Tokyo, Japan).

2.4. Energy absorption characterization under static loading

Uniaxial quasi-static compression was performed with a universal testing machine (MTS 810, Capacity 100 kN, MTS Systems Corporation, Minnesota,
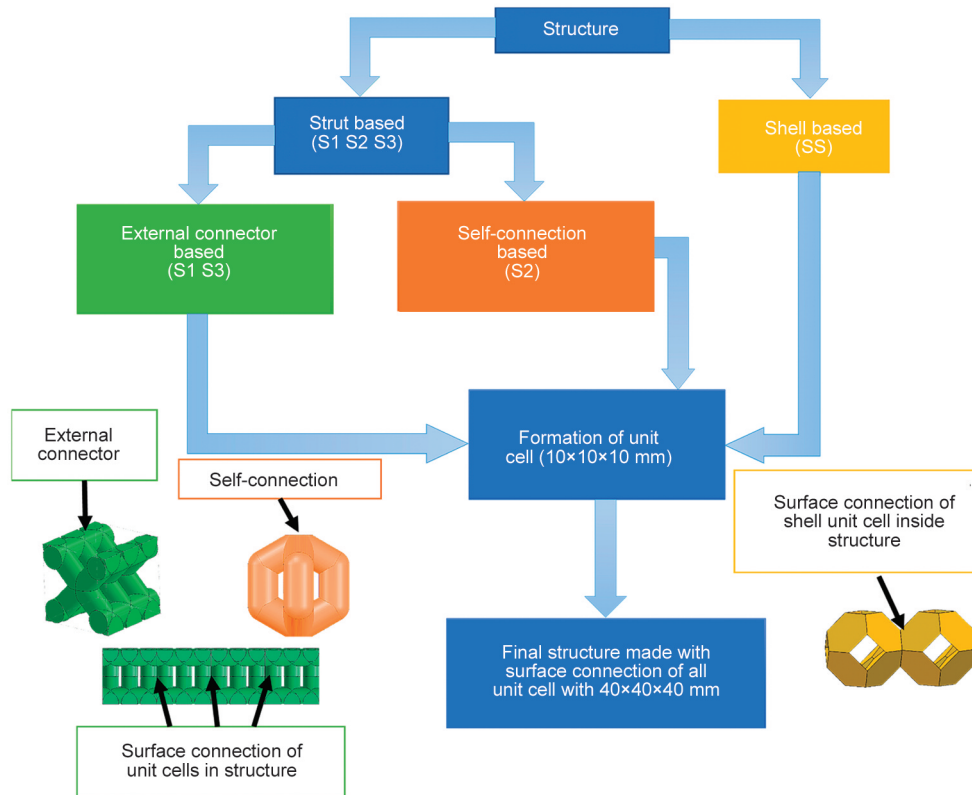
Figure 3. Unit cell assembly approach and final structure dimension.

Table 1. Optimized printing parameters used for manufacturing structures with FDM.

Material	Nozzle temperature [°C]	Printing speed [mm/s]	Heating bed temperature [°C]	Layer height [mm]	Infill density	Infill pattern
ABS	235	20	100	0.2	10%	Cubic
PLA	190	20	45	0.2	10%	Cubic

USA) to obtain the energy absorption capacity. All samples were compressed until failure. Here the meaning of failure is till the structure is delaminated or compressed to half of its depth. Compression plates were polished with oil to avoid samples sticking during compression. The test was conducted according to ASTM D1621 with a steady crossed-head speed of 3 mm/min under room temperature conditions [38]. All samples were compressed in the printing direction. To minimize biasing in the experiment, all structures were fabricated in large quantities, and three units of each structure were randomly tested. The energy absorption was calculated from the area under the load-displacement curve with OriginPro 2021 software (OriginLab Corporation, Northampton, USA). The value of the specific energy absorption (SEA) was calculated according to Equation (1) [39, 40]. Furthermore, the load-displacement data was converted into stress and strain to calculate the modulus. For further comparison purposes, these values were also normalized by relative density ($\bar{\rho}$),

which normalized the effect of materials and structural density. The relative density is defined as the ratio of structural density to the parent material density and is calculated as per Equation (2) [41]. The modulus per unit relative density is called relative modulus. Similarly, initial peak stress and energy absorbed per unit relative density is known as the relative initial peak stress and relative energy absorption, respectively.

$$SEA\,[\mathrm{J/g}] = \int_{0}^{\delta} \frac{F \cdot \mathrm{d}\delta}{w} \tag{1}$$

where w is the mass of the sample in grams, F is the compression force and $\mathrm{d}\delta$ is the displacement.

$$Relative\ density,\ \bar{\rho} = \frac{\rho}{\rho_s} \tag{2}$$

where ρ is the structural density, calculated with the ratio of the mass of the structure to the volume of the structure and ρ_s is the density of the parent material. The density of ABS and PLA was taken at 1.05 and

Table 2. Mass, volume, and relative density of FDM printed structures.

Material	Sample	Mass [g]	Volume [cm³]	Structure density [g/cm³]	Relative density, $\bar{\rho}$ [–]
ABS	S1	24.9	35.7	0.70	0.66
	S2	16.2	21.4	0.75	0.72
	S3	28.9	41.5	0.69	0.66
	SS	19.0	24.2	0.78	0.74
PLA	S1	29.0	35.7	0.81	0.66
	S2	19.0	21.4	0.89	0.72
	S3	33.6	41.5	0.81	0.66
	SS	22.6	24.2	0.93	0.75

1.24 g/cm³, respectively, from the literature [22]. Table 2 provides the mass of each sample, the material volume of the structures (calculated with Solidworks 2019), and structural and relative densities.

2.5. Dynamic compression

Because the structures were brittle and hard, sustaining the structures for repeated cycles was difficult. Hence, to perform the repeated compression, the cyclic displacement was required to be below the first peak point in the load-displacement curve during static testing. Moreover, during static testing, the displacement value of the first peak was considered to decide the range of the dynamic displacement. The displacement was given in the form of a sinusoidal wave using the same machine used for static compression. The range of the sinusoidal displacement

was from 30 to 50% of the displacement value of the first peak for each load-displacement curve of a static test. The range was selected after many trial experiments to prevent the plate and sample from detaching during the cycle. The cyclic test was performed only on samples that provided higher energy absorption in the static test. Ten cycles were applied, and the 10th cycle was considered for further calculations. The sin wave displacement was generated at three different frequencies, and all structures were tested at frequencies of 0.1 Hz (low), 1.0 Hz (base), and 4.0 Hz (high). The dynamic elastic recovery (DER) ratio of the area under the unloading curve to the loading curve was calculated for each 10th cycle along with the hysteresis work (the area enclosed by the cyclic curve).

3. Results and discussion
3.1. Surface integrity of the 3D-printed structure

To determine the integrity of the extruded layers, all samples were enlarged under an optical microscope. As observed in Figure 4, all layers were well connected and aligned. This shows that the quality of the 3D-printed structures was appropriate for compression testing. None of the samples demonstrated any visible type of void under extrusion, void cracking, or printing misalignment. For further verification, the samples were magnified under SEM. As can be seen from the SEM images, the extruded layers are
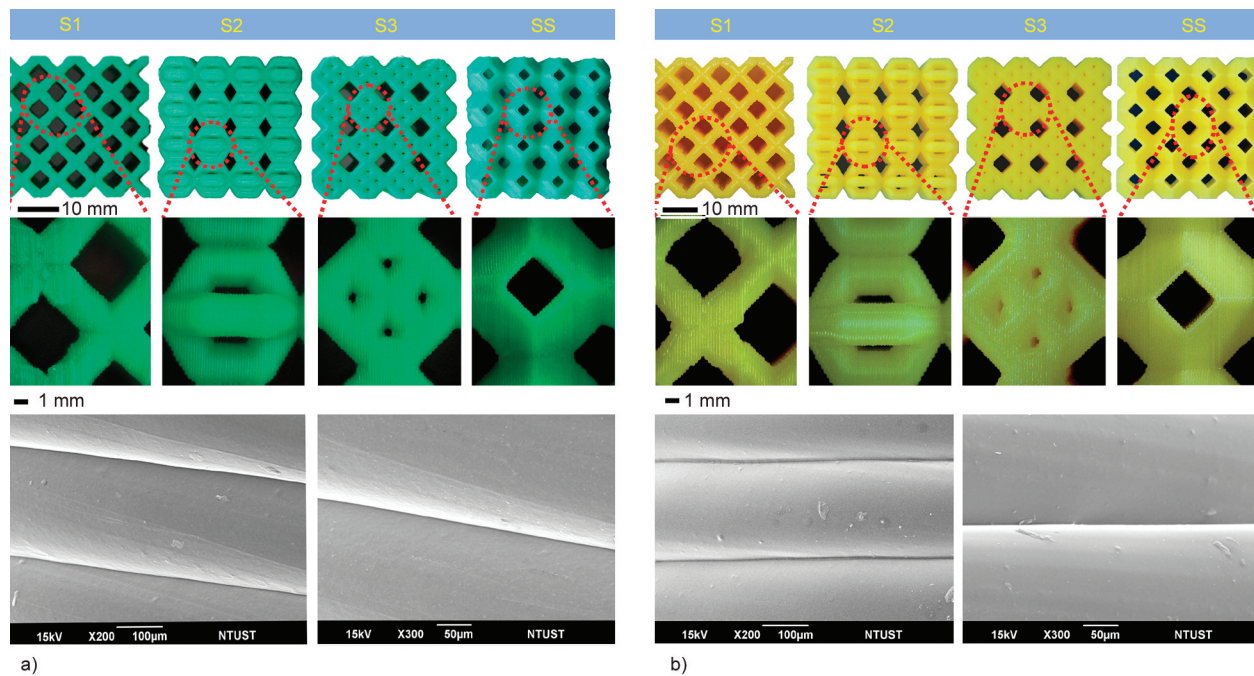
Figure 4. Layer integrity and quality of the extruded layers under high magnification SEM a) ABS, b) PLA.

firmly fused together at the interface without any delamination. At 200× magnification, the structure looks similar to an image captured by a light microscope. Further magnified to 300 times, the interface between the layers is still well bonded, and there are no microcracks and microvoids on the surface of the layer. This indicates that the print quality is fully up to standard and the sample is well-qualified for further testing. However, the interlayer adhesion strength of the samples needs to be tested under a universal testing machine.

3.2. Specific energy absorption under static loading

All structures exhibited different SEAs and initial peak values in load-displacement curves despite being composed of the same materials. Figure 5 depicts the load displacement of the S1 structures. Both material structures provided similar fluctuating curves regardless of the material. The PLA structure absorbed 4.71 J/g energy, whereas the ABS structure absorbed 1.99 J/g. The SEA for the PLA structure was 58% more than that of the ABS structure. The S1 structures (ABS and PLA) exhibited dominating stretching. Both structures experienced a cross-shear failure until the first curve, but this failure was more severely pronounced in the ABS structure owing to the delamination of the layers. The first peak for the PLA was higher than that of ABS because, until the first peak in the PLA structure, only some cracks were evident, in contrast, with ABS, the delamination had already started. After the first peak, the PLA structure showed cross-shear failure, which caused the large drop in the curve. However, subsequently, the structural part below the shear line exhibited resistance to the subsequent load. Therefore, the structure could sustain and carry the additional load. Owing to this, the PLA structure showed the second peak.
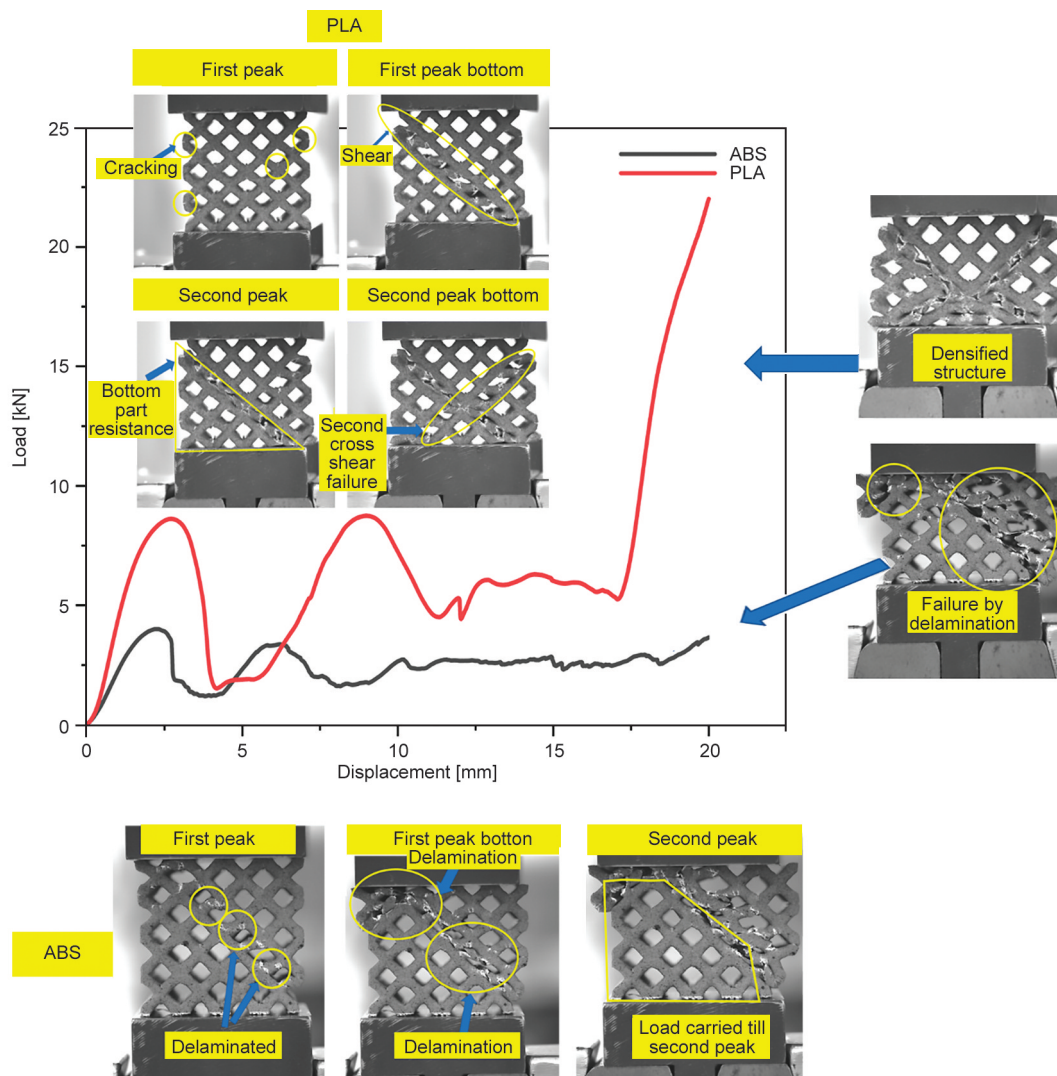

Figure 5. Load-displacement curve of S1 structure for ABS and PLA materials along with failure images at the different stages of static displacement.

After the second peak, one more cross-shear failure occurred, causing the second peak drop. After this point, the structure had already failed, but the debris of the structure carried the additional load from the bottom of the second peak and fully densified until the end.

For the ABS structure, after the first peak, the curve drop was a straight line because of the fatal delamination. Subsequently, the remaining structure was able to carry the load, thereby showing the second peak, but the structure failed with delamination. After the second drop in the peak, the next curve was caused by the debris of the structure. The delamination of the printed layer was the primary reason for the poor performance of the S1 structure with ABS.

A similar tendency was observed for the S2 structure, as shown by Figure 6, where the PLA structure had an of 6.87 J/g, which was 78% higher than that of the ABS structure, which was 1.51 J/g. However, the structures showed no fluctuations in the curve after the first peak. The ABS structure had broken from the bottom side until the first peak, whereas the PLA structure showed only some cracking, which caused a higher first-peak value for the PLA structure than that of the ABS structures. After the first peak, the

ABS structure was fully delaminated and could barely sustain until the 20 mm displacement owing to a complete debonding of the printed layer, whereas the PLA structure demonstrated a layer collapse.

For the S3 structures, as shown in Figure 7, regardless of the materials, both structures (ABS and PLA) showed the highest SEAs with 15.16 and 10.07 J/g for PLA and ABS, respectively. However, PLA still absorbed 34% more specific energy than the structures composed of ABS. These structures carried the load with a bending domination behavior in both materials. From the failure images, cracking and delamination started in the ABS structures until the first peak, whereas the PLA structure exhibited no signs of delamination. As the displacement progressed, the cracks formed in more areas in the ABS structure, whereas PLA deformed with collapsing layers. At the 20 mm displacement, the ABS structure showed a delamination failure, whereas the PLA structure failed by only a layer collapse. Here, layer debonding was also the cause of less energy absorbed by the ABS-printed structures.

Similarly, for the SS structures, the energy absorption was 6.29 and 3.16 J/g for the PLA and ABS structures, respectively. The SEA for PLA was still
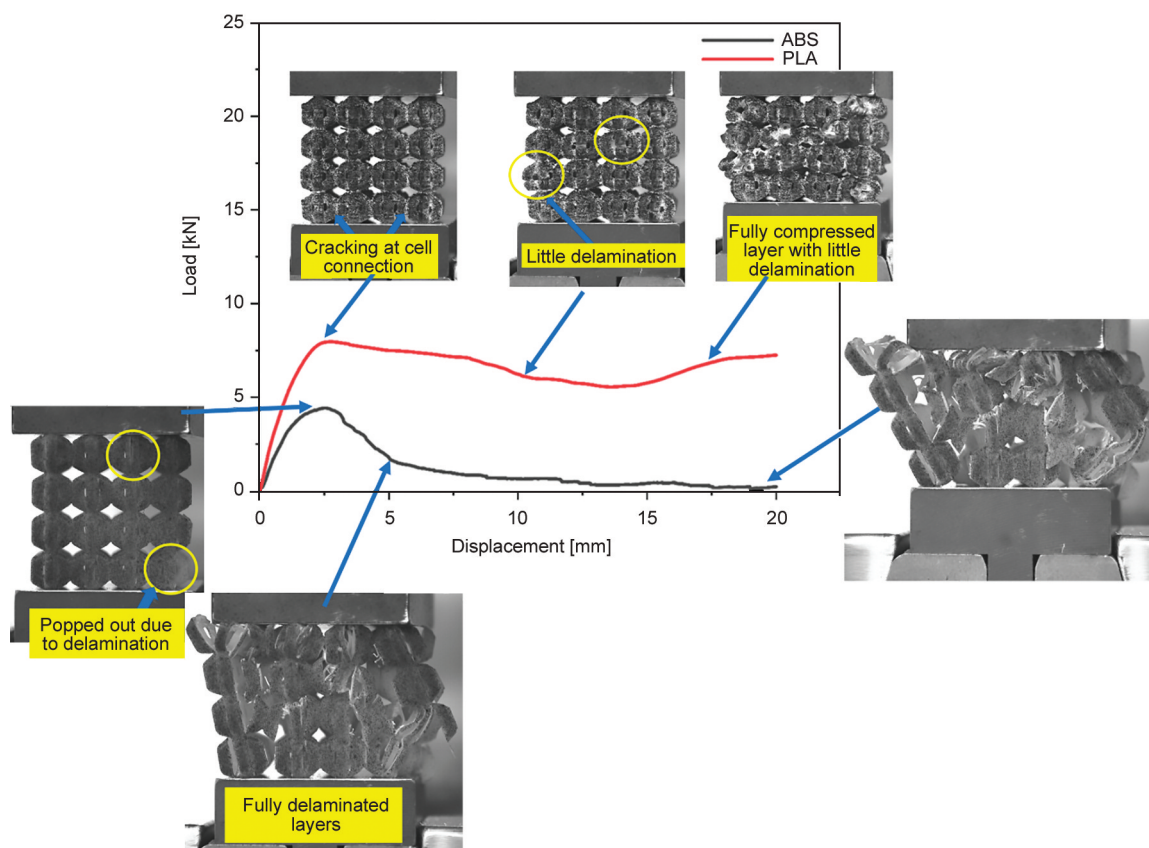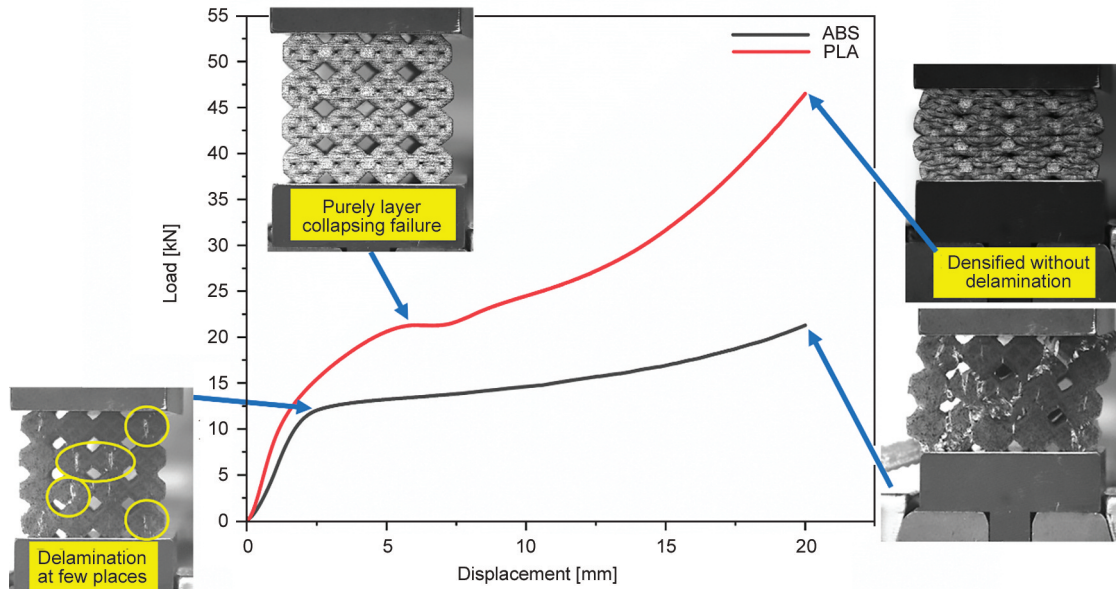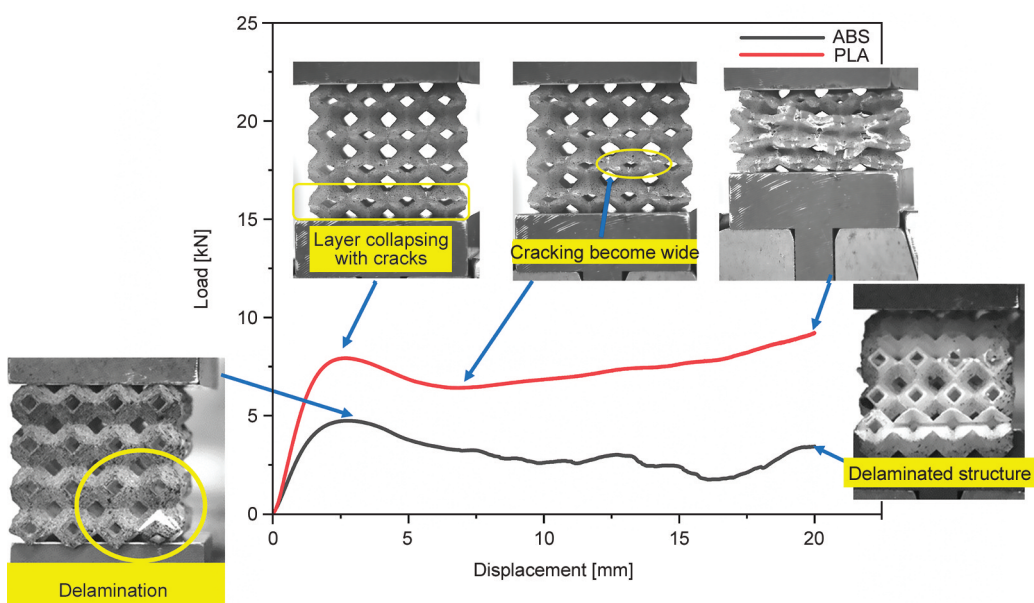

Figure 6. The load-displacement curve of S2 structure for ABS and PLA materials, along with failure images at the different stages of static displacement.

Figure 7. Load-displacement curve of S3 structure for ABS and PLA materials along with failure images at the different stages of static displacement.

50% higher than that of ABS. As shown in Figure 8, the structural effect provided the bending domination behavior. From the failure images until the first peak, the PLA structure failed because the bottom layers collapsed, but ABS had already delaminated severely. The PLA structure showed mostly layer-collapsing failures with small cracks. Hence, it was able to absorb more energy. In this case, the ABS structure demonstrated poor energy absorption because of the delamination. A small fluctuation was observed at the end of the ABS curve caused by the instability of the delaminated structure during compression.

To analyze the unit load required for unit displacement, the specific elastic constant of all structures was calculated from their respective load-displacement diagrams, as shown in Figure 9. The S3 structure had the highest specific elastic constant among all the PLA structures, followed by the S2 and SS structures, regardless of the material, and the S1 structure had the lowest specific elastic constant for both materials. Comparing the materials, the PLA structure had higher specific elastic constant values than those of the ABS structures. The poor interlayer adhesion for the ABS structure led to lower specific

Figure 8. The load-displacement curve of SS structure for ABS and PLA materials, along with failure images at the different stages of static displacemen.
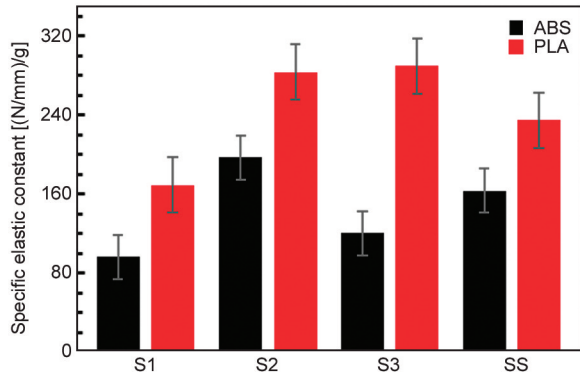
Figure 9. Specific elastic constant under static load calculated from the load-displacement diagrams.

Table 3. Specific modulus and specific initial peak stress under static loading.

Structures	Specific modulus [MPa/g]		Specific initial peak stress [MPa/g]	
	ABS	**PLA**	**ABS**	**PLA**
S1	1.45±0.06	1.53±0.70	0.10±0.01	0.19±0.02
S2	5.10±0.21	6.89±0.62	0.17±0.02	0.26±0.03
S3	3.14±0.03	5.26±0.99	0.27±0.03	0.40±0.06
SS	3.48±0.08	3.47±0.54	0.16±0.01	0.22±0.02

elastic constant values. As the S3 structure with PLA had the highest specific elastic constant, it required the highest amount of force to deform and could absorb more compression energy than the other structures. For the PLA structures, the energy absorption tendency agreed with the specific elastic constant value, but the early delamination for the ABS structures caused a deviation of the stiffness tendency from the energy absorption values.

The structural effect on the materials was also confirmed by the specific modulus and specific initial peak stress values calculated from the stress-strain curve, as shown in Figure 10. Table 3 lists the specific values of the respective structures. The structures showed different specific moduli and specific initial peak stresses. From this, a single material could provide several specific modulus and initial peak stress values depending on its structural arrangement. The failure mode of the structures would be the critical criterion for structural performance. The S3 structure with PLA had the highest SEA and

specific initial peak stress. Because the failure was purely dominated by layers collapsing for PLA, the same structure with ABS showed lower energy absorption and modulus values because of delamination. The S2 structure had the highest modulus for the PLA structure, but later little delamination in the structure caused lower energy absorption than S3 in the later stage. The S1 structure showed the lowest specific modulus for both material structures because of the diagonal shear failure.

For further comparisons, all values were normalized with the relative density of the respective structures. Table 4 lists the relative modulus, relative initial peak stress, and relative energy absorption. All structures with ABS showed lower values when compared with the structures with PLA. Structure S3 with PLA absorbed the highest relative energy and showed the highest relative modulus and the highest relative initial peak stress. All other structures S1, S2 and SS provided lower values when compared with the S3 structure of PLA. The cause of the higher performance of the S3 structure with PLA was also described on the base of failure mode, which was a complete layer-wise collapsing failure. All other
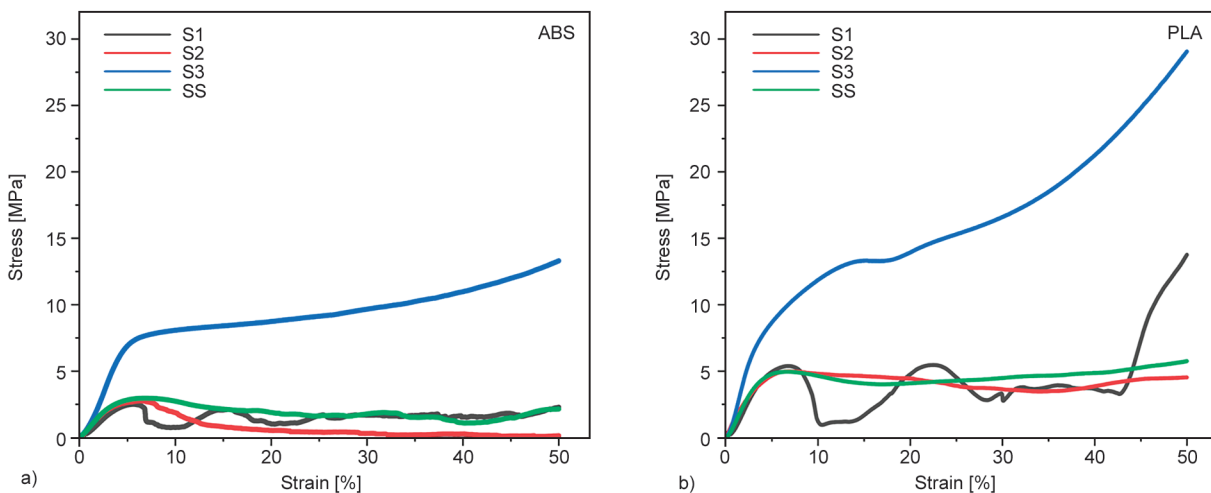

Figure 10. Stress-strain curves of the structures under the static loading. a) ABS, b) PLA.

Table 4. Relative modulus, relative initial peak stress, and relative energy absorption of structures under static loading.

Structures	Relative modulus [MPa]		Relative initial peak stress [MPa]		Relative energy absorption [J]	
	ABS	**PLA**	**ABS**	**PLA**	**ABS**	**PLA**
S1	54.70±2.22	67.14±0.55	3.81±0.03	8.17±0.29	74.98±4.08	206.67±2.50
S2	114.84±3.35	181.76 ±0.58	3.85±0.05	6.92±0.04	33.73±0.66	180.81±0.39
S3	137.50±1.18	267.84±0.63	11.60±0.14	20.13±0.05	440.40±2.02	772.35±0.06
SS	88.08±2.55	104.38±0.06	4.01±0.02	6.61±0.06	79.89±0.38	192.25±0.25

structures, showed little delamination in the case of PLA structures and severe delamination was observed with ABS structures.

Overall, from Figures 5 to 8, the load-displacement curve for the ABS structures was lower in all cases. The root cause of the poor performance of the ABS structures was the delamination of the printed layers under compression. The dominant failure mode for ABS structures was cracking, followed by fatal delamination, which was less pronounced in PLA structures. The S3 structures with PLA absorbed the highest energy because the mode failed purely from collapsing layers. Hence, for a good 3D printed structure, better interlayer adhesion is highly necessary. In a general case, ABS is stiffer than PLA, but the structural effect reversed the nature of the materials. All structures absorbed different amounts of energy and showed different elastic moduli and initial peak stresses, regardless of the material, which indicates that a material can have a wide energy absorption capacity range under compression loading that can be altered by changing the structural arrangement. That is, the structure and its integrity can determine the mechanical energy absorption capacity of the constituent materials. For ABS, FDM fails to achieve good layer adhesion, which can be attributed to the rapid consolidation reducing the interfacial layer adhesion ability. However, it is not as pronounced as in the case of crystalline PLA.

3.3. Energy absorption by structures under dynamic displacement

The PLA structure outperformed ABS structures because of better inter-layer adhesion. Hence, only PLA structures were selected for dynamic cyclic compression. Figure 11 shows the 10th load displacement cycles of each structure at the base frequency (1.0 Hz). The other cycles had similar enclosure shapes; hence, for the other two frequencies, only the DER and hysteresis work are reported in Table 5 for the 10th cycle.

As presented in Table 5, PLA showed different DER values for all frequencies, because of the structural effect. Hence, the DER of the materials could be determined by structural arrangement. Here, the structures were first tested at the base frequency of 1.0 Hz. At this frequency, the S3 structure showed the lowest DER, whereas the SS structure provided the highest DER of 96.12%. The S1 and S2 structures had DERs of 92.31 and 95.63%, respectively. DER generally indicates the amount of recovery that occurs after cyclic loading. A higher dynamic recovery means a higher energy-releasing ability, and vice-versa. The S3 structure stored the highest hysteresis work, which indicates that this structure had a higher ability for storing energy than that for release. Moreover, the SS structure was able to release energy better than all other structures and could store only 0.08 J of hysteresis work. By comparing the SS and S2 structures, the difference in DER was 0.50%, and the hysteresis works were the same.

When testing at the low frequency (0.1 Hz), all structures followed the same tendency as with the base frequency in terms of DER and stored hysteresis work. The lowest DER and highest hysteresis work were provided by the S3 structure. The SS structure had the best DER of approximately 96.52% with the lowest hysteresis work of 0.07 J. The S2 and S1 structures had DERs of 94.48 and 93.31% with hysteresis works of 0.09 and 0.17 J. At this frequency, the S3 structures had similar behaviors as those observed at the base frequency. Comparing all structures at 1.0 and 0.1 Hz, all structures demonstrated similar DERs, hence, the frequency change did not significantly affect the DER or the hysterics work at a larger scale to differ with a small range.

On testing all structures at the high frequency (4.0 Hz), the S3 structure showed the lowest DER again, along with the highest hysteresis work at 1.48 J. The SS structures had a DER of 97.13%, which was the highest among all structures. The S2 and S1 structures had the second and third best
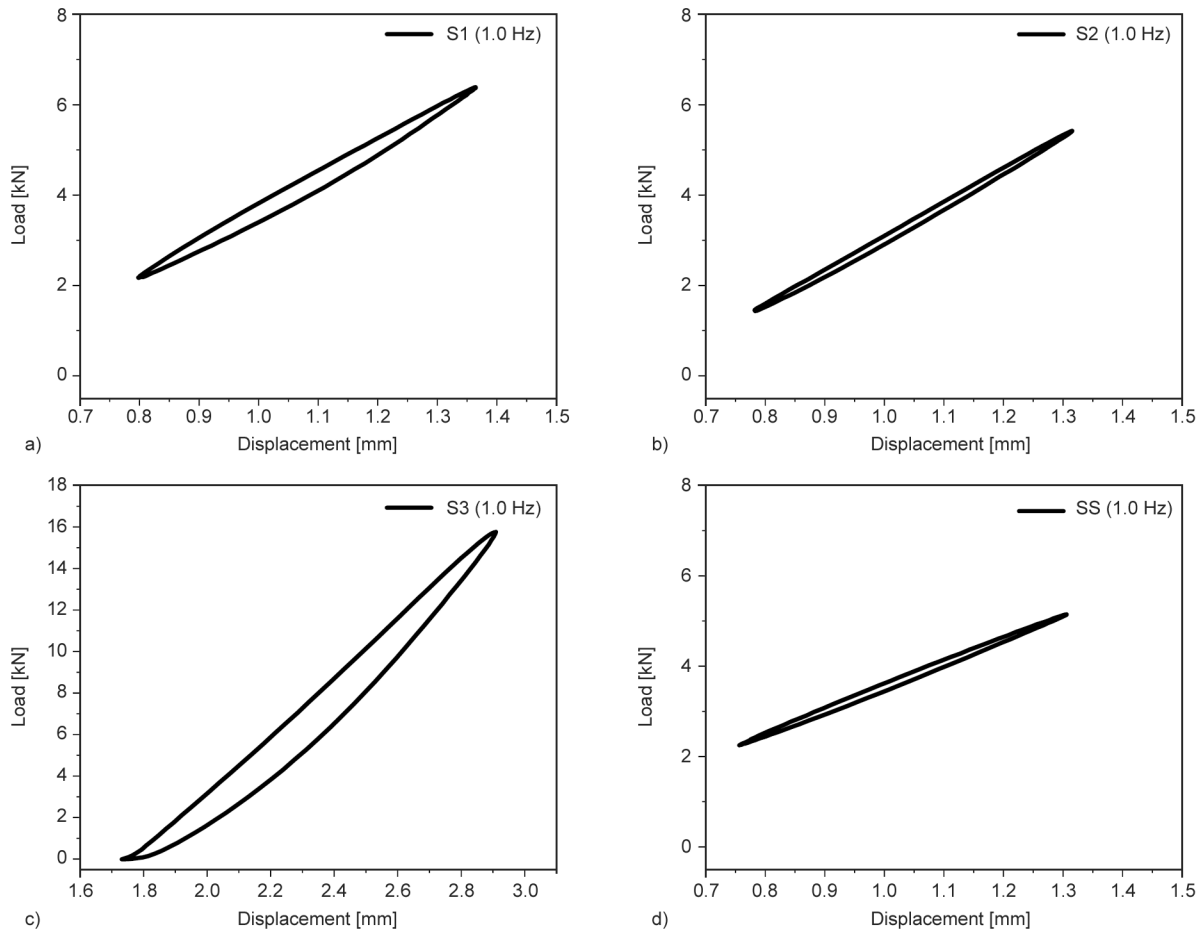
Figure 11. 10th load displacement cycle of each structure under dynamic loading at the base frequency (1.0 Hz). a) S1, b) S2, c) S3, d) SS.

Table 5. DER and hysteresis work of PLA structures under dynamic loading.

Structures	Frequency 0.1 Hz		Frequency 1.0 Hz		Frequency 4.0 Hz	
	DER [%]	Hysteresis work [J]	DER [%]	Hysteresis work [J]	DER [%]	Hysteresis work [J]
S1	93.31	0.17	92.31	0.19	93.46	0.20
S2	94.48	0.09	95.63	0.08	96.81	0.08
S3	80.45	1.14	79.62	1.91	85.94	1.48
SS	96.52	0.07	96.12	0.08	97.13	0.07

DERs of 96.81 and 93.46%, respectively. At this frequency, the DER of all structures was the highest compared with the DER responses at 0.1 and 1.0 Hz. At all frequencies, the S3 structure had the lowest DER but the highest hysteresis work absorbed. The cause of the high value of hysteresis work absorption could be explained based on the free volume of the structures. The S3 structure consisted of the most material, thereby having the lowest free volume. The struts were close to each other, which provided better support for the applied loading. Less free space for the movement of struts in S3 enabled it to sustain a high loading but made its elastic recovery poor. Similarly, the S1 structure had the second heaviest structure and more free volume than the S3 structure. Owing to the higher free volume, the structure could recover more because of a better release of energy; hence, less hysteresis work was observed than with S3. The S2 structure had the lowest amount of material among the strut-type structures. The additional free volume in the S2 structure provided more movement space for the structures while loading. Because of the additional free space, the struts in the S2 structure were able to recover better for all frequencies. The S2 was the best in terms of DER among the strut-type structures.

The SS structure had shell unit cells. The space for movement inside shell is more, which means more

free space for the movement of shells. The free volume of the SS structure enabled them to reach the highest DER with the lowest hysteresis work absorption. For a structure, the free volume is a significant factor in determining the DER and hysteresis work absorption at all frequencies. Here, the S3 structure is recommended for better energy absorption applications. The SS structure is recommended for applications requiring a quicker recovery under dynamic loading conditions. The S3 and SS structures had large DER and hysteresis work differences but a small difference was observed in the DER and hysteresis work when these structures were individually compared at different frequencies. Hence, the DER and hysteresis work was more pronounced with the structural change rather than the frequency change.

## 3.4. Effect of frequency on the structural damping ability

The damping ability of the structures was calculated from the lag (δ) between the dynamic load and displacement curves, as shown in Figure 12. The tangent of the lag (tan δ) indicates the damping ability of the structures. Table 6 provides the average tan δ of the 10 cycles and the tan δ of the strut-structures

Table 6. Average tan δ of 10 cycles at different frequencies (0.1, 1.0, 4.0 Hz).

Structures	tan δ·10⁻²		
	0.1 Hz	**1.0 Hz**	**4.0 Hz**
S1	2.13	2.43	3.82
S2	2.05	2.99	3.82
S3	3.36	3.61	3.82
SS	1.93	2.43	1.05

(S1, S2, S3) and SSs. For strut-based structures, as the frequency was increased from 0.1 to 4.0 Hz, the tan δ increased for the S1, S2, and S3 structures. The S3 structure had the highest tan δ, indicating that this structure had a more viscous nature and provided the lowest DER because it could dissipate the energy as hysteresis work. The SSs had the lowest tan δ, which shows that these structures had a more elastic nature and highest DER.

By comparing the frequency effect, based on the viscoelastic nature of materials [42], materials become brittle at high frequencies and viscous at low frequencies. However, owing to the structural effect, strut-based structures (S1, S2, and S3) showed a more viscous nature at a high frequency. This indicates that the nature of the material could be changed
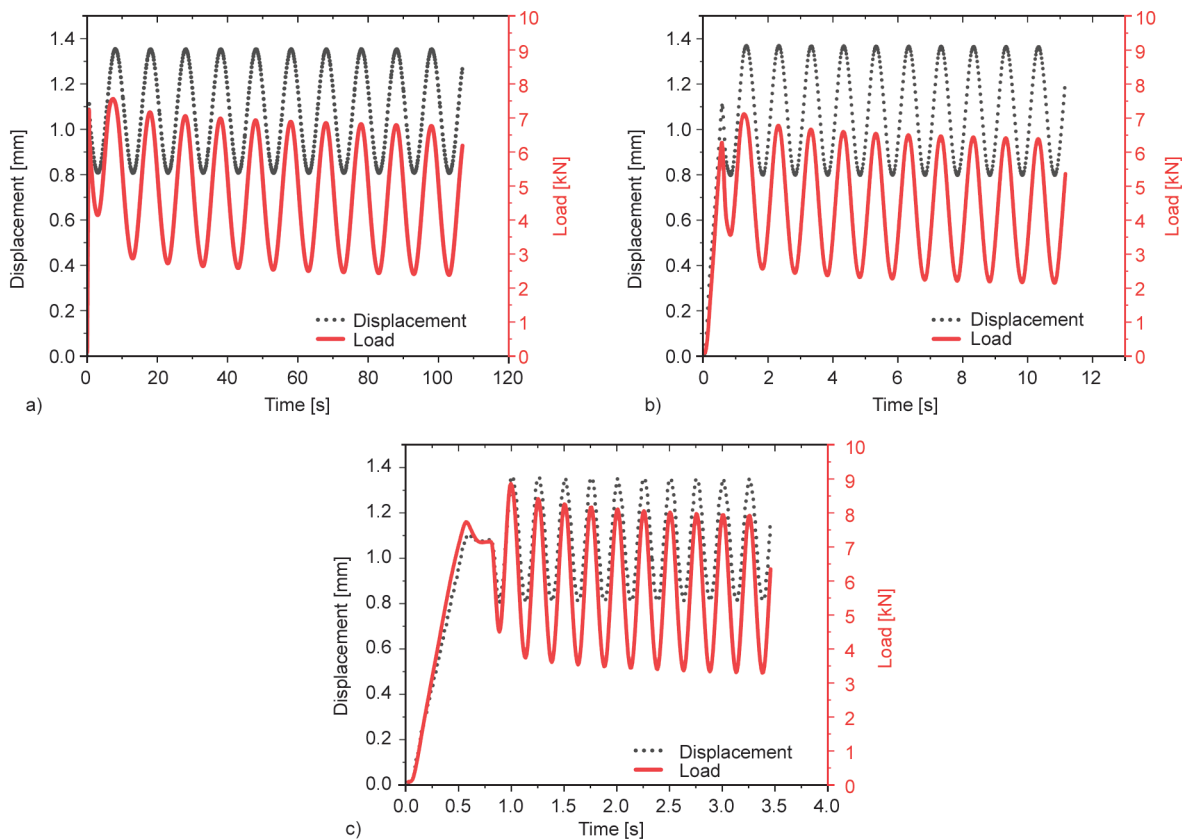
Figure 12. Load-time-displacement diagrams for S1 structures under dynamic loading at a) 0.1 Hz, b) 1.0 Hz, and c) 4.0 Hz.

Table 7. Percentage improvement in energy absorption of S3 (ABS and PLA) structures compared with previously reported FDM fabricated structures.

Structure	Material	Energy absorbed [J/g]	Improvement [%]	References
Honeycomb	ABS	5.43	46	[22]
Hexagonal re-entrant		2.82	72	[41]
Tet oct vertex centroid		2.63	74	[45]
Body center cube-V		0.49	95	[46]
Biomorphic cellular		1.50	85	[47]
Modified octet	PLA	4.50	70	[43]
Bi-graded honeycomb		13.62	10	[48]
Hexagonal prism		10.50	30	[49]
Kelvin foams		11.90	21	[50]
Neovius surface		10.42	31	[51]

by changing the material arrangement in the structures. The structural effect can also be justified by the ability to transmit vibration out of the system. The high tan δ indicates a higher damping property. The many interconnected struts composing the structures helped transmit the vibration out of the structures. At the lower frequency, the struts moved slowly; thus, less vibration was transmitted out of the structures and caused less vibration isolation. Therefore, a low tan δ was obtained at the high frequency because the fast movement of the struts made the structures transmit more vibration out. The surfaces of the SSs could not provide as much movement as the struts, obtaining a low tan δ at the higher frequency. All structures composed of struts could be applied at the higher frequency vibration damping, but the SS structure composed of the surface is better suited for lower frequency vibrational damping applications.

3.5. Comparison of failure mode and energy absorption results

For the S3 structure, PLA absorbed the highest amount of energy because of the full layer collapsing failure. The upper and lower layers started deforming, and this deformation traveled toward the center layer without delamination and ended with densification of the structure without layer debonding during the entire compression period. A comparison of the S3 failure mode with the octet structures with PLA studied by [43] showed that the collapsing deformation of the unstable layer caused the post-yield fluctuation behavior. Hence, the energy absorption was approximately 87% less than that of the S3 structure with PLA. This shows that stability in layer collapsing is essential for structure deformation. Another study reported a re-entrant circular auxetic

honeycomb structure [44] from PLA material, demonstrating non-uniform cross X-like failure during compression. Moreover, owing to this type of failure, the oscillation formed into a stress-strain curve, and the highest SEA was reported at only 2.2 J/g, which is far less than that of the S3 structure. Similarly, another study [35] with a hexagonal open cell structure composed of PLA showed that the best stress-strain curve was obtained with a structure with a layer collapsing failure. These results agree with the cause of the highest energy absorption observed for the S3 structure. The cross failure by the S1 structure for both materials is undesirable, and this also agrees with the deformation behavior explained by [44]. Other structures, S2 and SS, showed minimal delamination with PLA and were severely delaminated with the ABS material which caused the poor SEA results for ABS. This result agrees with [26], which stated that the structure with little debonding had the highest mechanical properties. Comprehensively, the layer collapsing mode with a stable manner is the best deformation mode for 3D-printed structures, whereas debonding always reduces the performance of these types of structures.

To analyze the improvement of the purposed structure, the result of the energy absorption of bending-dominated S3 structures was compared with the results published in the literature, as listed in Table 7 for ABS and PLA.

4. Conclusions
- The structural effect changed the energy absorption of the materials (PLA and ABS). A material can absorb different amounts of energy under compression, which can be determined by structural arrangements.

- For FDM-manufactured structures, interlayer adhesion plays the main role in energy absorption under compression. ABS could not provide better layer adhesion; hence, delamination caused it to absorb less energy than the PLA structures.
- The results show that the energy absorbed by the S3 structure of PLA is the highest, which is 15.16 J/g, the specific strength of the first peak is the highest, which is 0.40 MPa/g, and relative modulus is the highest, which is 267.84 MPa.
- The free volume of the structures resulted in a quick recovery after dynamic loading.
- Under dynamic compression, changes in frequency were less effective for the DER, but the structural change effect was more pronounced on the DER and hysteresis work.
- The SS structure has the best dynamic elastic recovery of 97.13% at 4.0 Hz, while S3 shows the best hysteretic work at 1.91 J.
- All strut-based structures demonstrated a viscous nature at a high frequency, whereas a more elastic nature was observed in the SSs.
- The bending-dominated (S3) structures are recommended for civil engineering applications, such as in load bearing, SS has the highest DER; hence, they can be used for applications requiring quick recovery after loading.

Acknowledgements

References
[1] Liu G., Zhang X., Chen X., He Y., Cheng L., Huo M., Yin J., Hao F., Chen S., Wang P., Yi S., Wan L., Mao Z., Chen Z., Wang X., Cao Z., Lu J.: Additive manufacturing of structural materials. Materials Science and Engineering R: Reports, **145**, 100596 (2021).
https://doi.org/10.1016/j.mser.2020.100596

[2] Maconachie T., Leary M., Lozanovski B., Zhang X., Qian M., Faruque O., Brandt M.: SLM lattice structures: Properties, performance, applications and challenges. Materials and Design, **183**, 108137 (2019).
https://doi.org/10.1016/j.matdes.2019.108137

[3] Tyagi S., Yadav A., Deshmukh S.: Review on mechanical characterization of 3D printed parts created using material jetting process. Materials Today: Proceedings, **51**, 1012–1016 (2021).
https://doi.org/10.1016/j.matpr.2021.07.073

[4] Piedra-Cascón W., Krishnamurthy V. R., Att W., Revilla-León M.: 3D printing parameters, supporting structures, slicing, and post-processing procedures of vat-polymerization additive manufacturing technologies: A narrative review. Journal of Dentistry, **109**, 103630 (2021).
https://doi.org/10.1016/j.jdent.2021.103630

[5] Gupta A. K., Krishnanand, Taufik M.: The effect of process parameters in material extrusion processes on the part surface quality: A review. Materials Today: Proceedings, **50**, 1234–1242 (2021).
https://doi.org/10.1016/j.matpr.2021.08.110

[6] Chua C. K., Wong C. H., Yeong W. Y.: Material characterization for additive manufacturing. in 'Standards, quality control, and measurement sciences in 3D printing and additive manufacturing' (eds.: Chua C. K., Wong C. H., Yeong W. Y.) Academic Press, London, 95–137 (2017).
https://doi.org/10.1016/B978-0-12-813489-4.00005-2

[7] Kumaran M., Senthilkumar V., Justus Panicker C. T., Shishir R.: Investigating the residual stress in additive manufacturing of combined process in powder bed fusion and directed energy deposition. Materials Today: Proceedings, **47**, 4387–4390 (2021).
https://doi.org/10.1016/j.matpr.2021.05.200

[8] Li M., Huang J., Fang A., Mansoor B., Pei Z., Ma C.: Binder jetting additive manufacturing of copper/diamond composites: An experimental study. Journal of Manufacturing Processes, **70**, 205–213 (2021).
https://doi.org/10.1016/j.jmapro.2021.08.041

[9] Ullsperger T., Wencke Y. L., Yürekli B., Matthäus G., Rettenmayr M., Luinstra G. A., Nolte S.: Laser powder bed fusion of ultra-high molecular weight polyethylene (UHMWPE) using near-infrared ultrashort laser pulses. Materials and Design, **210**, 110048 (2021).
https://doi.org/10.1016/j.matdes.2021.110048

[10] Rowat S. J., Legge R. L., Moresoli C.: Plant protein in material extrusion 3D printing: Formation, plasticization, prospects, and challenges. Journal of Food Engineering, **308**, 110623 (2021).
https://doi.org/10.1016/j.jfoodeng.2021.110623

[11] Hanon M. M., Dobos J., Zsidai L.: The influence of 3D printing process parameters on the mechanical performance of PLA polymer and its correlation with hardness. Procedia Manufacturing, **54**, 244–249 (2020).
https://doi.org/10.1016/j.promfg.2021.07.038

[12] Wang P., Zou B., Ding S., Li L., Huang C.: Effects of FDM-3D printing parameters on mechanical properties and microstructure of CF/PEEK and GF/PEEK. Chinese Journal of Aeronautics, **34**, 236–246 (2021).
https://doi.org/10.1016/j.cja.2020.05.040

[13] Chikkangoudar R. N., Sachidananda T. G., Pattar N.: Influence of 3D printing parameters on the dimensional stability of polypropylene/clay printed parts using laser scanning technique. Materials Today: Proceedings, **44**, 4118–4123 (2020).
https://doi.org/10.1016/j.matpr.2020.10.456

[14] Prabhakar M. M., Saravanan A. K., Lenin A. H., Leno I. J., Mayandi K., Ramalingam P. S.: A short review on 3D printing methods, process parameters and materials. Materials Today: Proceedings, **45**, 6108–6114 (2020).
https://doi.org/10.1016/j.matpr.2020.10.225

[15] Liu Y., Bai W., Cheng X., Tian J., Wei D., Sun Y., Di P.: Effects of printing layer thickness on mechanical properties of 3D-printed custom trays. Journal of Prosthetic Dentistry, **126**, 671.e1–671.e7 (2020).
https://doi.org/10.1016/j.prosdent.2020.08.025

[16] Fekete I., Ronkay F., Lendvai L.: Highly toughened blends of poly(lactic acid) (PLA) and natural rubber (NR) for FDM-based 3D printing applications: The effect of composition and infill pattern. Polymer Testing, **99**, 107205 (2021).
https://doi.org/10.1016/j.polymertesting.2021.107205

[17] Park S., Fu K.: Polymer-based filament feedstock for additive manufacturing. Composites Science and Technology, **213**, 108876 (2021).
https://doi.org/10.1016/j.compscitech.2021.108876

[18] Elmrabet N., Siegkas P.: Dimensional considerations on the mechanical properties of 3D printed polymer parts. Polymer Testing, **90**, 106656 (2020).
https://doi.org/10.1016/j.polymertesting.2020.106656

[19] Liu C-H., Chen Y., Yang S-Y.: Quantification of hyperelastic material parameters for a 3D-Printed thermoplastic elastomer with different infill percentages. Materials Today Communications, **26**, 101895 (2021).
https://doi.org/10.1016/j.mtcomm.2020.101895

[20] Zhang P., Qi D., Xue R., Liu K., Wu W., Li Y.: Mechanical design and energy absorption performances of rational gradient lattice metamaterials. Composite Structures, **277**, 114606 (2021).
https://doi.org/10.1016/j.compstruct.2021.114606

[21] Kaur M., Yun T. G., Han S. M., Thomas E. L., Kim W. S.: 3D printed stretching-dominated micro-trusses. Materials and Design, **134**, 272–280 (2017).
https://doi.org/10.1016/j.matdes.2017.08.061

[22] Joseph A., Mahesh V., Mahesh V.: Effect of loading rates on the in-plane compressive properties of additively manufactured ABS and PLA-based hexagonal honeycomb structures. Journal of Thermoplastic Composite Materials, **10**, 1–22 (2021).
https://doi.org/10.1177/08927057211051416

[23] Sychov M. M., Lebedev L. A., Dyachenko S. V., Nefedova L. A.: Mechanical properties of energy-absorbing structures with triply periodic minimal surface topology. Acta Astronautica, **150**, 81–84 (2018).
https://doi.org/10.1016/j.actaastro.2017.12.034

[24] Gautam R., Idapalapati S., Feih S.: Printing and characterisation of Kagome lattice structures by fused deposition modelling. Materials and Design, **137**, 266–275 (2018).
https://doi.org/10.1016/j.matdes.2017.10.022

[25] Ye G., Bi H., Li Z., Hu Y.: Compression performances and failure modes of 3D printed pyramidal lattice truss composite structures. Composites Communications, **24**, 100615 (2021).
https://doi.org/10.1016/j.coco.2020.100615

[26] Dalaq A. S., Abueidda D. W., Abu Al-Rub R. K.: Mechanical properties of 3D printed interpenetrating phase composites with novel architectured 3D solid-sheet reinforcements. Composites Part A: Applied Science and Manufacturing, **84**, 266–280 (2016).
https://doi.org/10.1016/j.compositesa.2016.02.009

[27] Bates S. R. G., Farrow I. R., Trask R. S.: 3D printed polyurethane honeycombs for repeated tailored energy absorption. Materials and Design, **112**, 172–183 (2016).
https://doi.org/10.1016/j.matdes.2016.08.062

[28] Li T., Wang L.: Bending behavior of sandwich composite structures with tunable 3D-printed core materials. Composite Structures, **175**, 46–57 (2017).
https://doi.org/10.1016/j.compstruct.2017.05.001

[29] Abueidda D. W., Bakir M., Abu Al-Rub R. K., Bergström J. S., Sobh N. A., Jasiuk I.: Mechanical properties of 3D printed polymeric cellular materials with triply periodic minimal surface architectures. Materials and Design, **122**, 255–267 (2017).
https://doi.org/10.1016/j.matdes.2017.03.018

[30] Yazdani S. H., Akbarzadeh A. H., Mirbolghasemi A., Hermenean K.: 3D printed meta-sandwich structures: Failure mechanism, energy absorption and multi-hit capability. Materials and Design, **160**, 179–193 (2018).
https://doi.org/10.1016/j.matdes.2018.08.061

[31] Al-Ketan O., Rowshan R., Abu Al-Rub R. K.: Topology-mechanical property relationship of 3D printed strut, skeletal, and sheet based periodic metallic cellular materials. Additive Manufacturing, **19**, 167–183 (2018).
https://doi.org/10.1016/j.addma.2017.12.006

[32] Abueidda D. W., Elhebeary M., Shiang C-S., Pang S., Abu Al-Rub R. K., Jasiuk I. M.: Mechanical properties of 3D printed polymeric Gyroid cellular structures: Experimental and finite element study. Materials and Design, **165**, 107597 (2019).
https://doi.org/10.1016/j.matdes.2019.107597

[33] Ling C., Cernicchi A., Gilchrist M. D., Cardiff P.: Mechanical behaviour of additively-manufactured polymeric octet-truss lattice structures under quasi-static and dynamic compressive loading. Materials and Design, **162**, 106–118 (2019).
https://doi.org/10.1016/j.matdes.2018.11.035

[34] Li X., Kawai K., Fujitsuka M., Osakada Y.: COF-based photocatalyst for energy and environment applications. Surfaces and Interfaces, **25**, 101249 (2021).
https://doi.org/10.1016/j.surfin.2021.101249

[35] Ben Ali N., Khlif M., Hammami D., Bradai C.: Mechanical and morphological characterization of spherical cell porous structures manufactured using FDM process. Engineering Fracture Mechanics, **216**, 106527 (2019).
https://doi.org/10.1016/j.engfracmech.2019.106527

[36] Baumann A. E., Burns D. A., Liu B., Thoi V. S.: Metal-organic framework functionalization and design strategies for advanced electrochemical energy storage devices. Communications Chemistry, **2**, 86 (2019).
https://doi.org/10.1038/s42004-019-0184-6

[37] Chen L., Zhang X., Cheng X., Xie Z., Kuang Q., Zheng L.: The function of metal-organic frameworks in the application of MOF-based composites. Nanoscale Advances, **2**, 2628–2647 (2020).
https://doi.org/10.1039/D0NA00184H

[38] Miralbes R., Ranz D., Pascual F. J., Zouzias D., Maza M.: Characterization of additively manufactured triply periodic minimal surface structures under compressive loading. Mechanics of Advanced Materials and Structures, **29**, 1841–1855 (2020).
https://doi.org/10.1080/15376494.2020.1842948

[39] Alkateb M., Sapuan S. M., Leman Z., Jawaid M., Ishak M. R.: Quasi-static crush behaviour of environmentally friendly kenaf/wool epoxy composites elliptical tube. Journal of Mechanical Engineering and Sciences, **12**, 3671–3688 (2018).
https://doi.org/10.15282/jmes.12.2.2018.13.0325

[40] Zeng C., Liu L., Bian W., Leng J., Liu Y.: Bending performance and failure behavior of 3D printed continuous fiber reinforced composite corrugated sandwich structures with shape memory capability. Composite Structures, **262**, 113626 (2021).
https://doi.org/10.1016/j.compstruct.2021.113626

[41] Choudhry N. K., Panda B., Kumar S.: In-plane energy absorption characteristics of a modified re-entrant auxetic structure fabricated via 3D printing. Composites Part B: Engineering, **228**, 109437 (2022).
https://doi.org/10.1016/j.compositesb.2021.109437

[42] Mills N., Jenkins M., Kukureka S.: Viscoelastic behaviour. in 'Plastics: Microstructure and engineering applications' (eds.: Mills N., Jenkins M., Kukureka S.) Butterworth-Heinemann, Oxford, 111–125 (2020).
https://doi.org/10.1016/B978-0-08-102499-7.00007-2

[43] Sun Z. P., Guo Y. B., Shim V. P. W.: Characterisation and modeling of additively-manufactured polymeric hybrid lattice structures for energy absorption. International Journal of Mechanical Sciences, **191**, 106101 (2021).
https://doi.org/10.1016/j.ijmecsci.2020.106101

[44] Qi C., Jiang F., Remennikov A., Pei L-Z., Liu J., Wang J-S., Liao X-W., Yang S.: Quasi-static crushing behavior of novel re-entrant circular auxetic honeycombs. Composites Part B: Engineering, **197**, 108117 (2020).
https://doi.org/10.1016/j.compositesb.2020.108117

[45] Silva R. G., Torres M. J., Viñuela J. Z., Zamora A. G.: Manufacturing and characterization of 3D miniature polymer lattice structures using fused filament fabrication. Polymers, **13**, 635 (2021).
https://doi.org/10.3390/polym13040635

[46] Fadeel A., Mian A., Al Rifaie M., Srinivasan R.: Effect of vertical strut arrangements on compression characteristics of 3D printed polymer lattice structures: Experimental and computational study. Journal of Materials Engineering and Performance, **28**, 709–716 (2019).
https://doi.org/10.1007/s11665-018-3810-z

[47] Ufodike C. O., Ahmed M. F., Dolzyk G.: Additively manufactured biomorphic cellular structures inspired by wood microstructure. Journal of the Mechanical Behavior of Biomedical Materials, **123**, 104729 (2021).
https://doi.org/10.1016/j.jmbbm.2021.104729

[48] Wu Y., Sun L., Yang P., Fang J., Li W.: Energy absorption of additively manufactured functionally bi-graded thickness honeycombs subjected to axial loads. Thin-Walled Structures, **164**, 107810 (2021).
https://doi.org/10.1016/j.tws.2021.107810

[49] Wang S., Zheng Z., Zhu C., Ding Y., Yu J.: Crushing and densification of rapid prototyping polylactide foam: Meso-structural effect and a statistical constitutive model. Mechanics of Materials, **127**, 65–76 (2018).
https://doi.org/10.1016/j.mechmat.2018.09.003

[50] Duan Y., Du B., Shi X., Hou B., Li Y.: Quasi-static and dynamic compressive properties and deformation mechanisms of 3D printed polymeric cellular structures with Kelvin cells. International Journal of Impact Engineering, **132**, 103303 (2019).
https://doi.org/10.1016/j.ijimpeng.2019.05.017

[51] Sychov M. M., Lebedev L. A., Dyachenko S. V., Nefedova L. A.: Mechanical properties of energy-absorbing structures with triply periodic minimal surface topology. Acta Astronautica, **150**, 81–84 (2018).
https://doi.org/10.1016/j.actaastro.2017.12.034